Available online at www.sciencedirect.com

ScienceDirect

Cement and Concrete Research 36 (2006) 2061 – 2073

Cement and Concrete Research

A polydispersed particle system representation of the porosity for non-saturated cementitious materials

B. Bary *

CEA Saclay, DEN/DPC/SCCME/LECBA, 91191 Gif/Yvette, France

Received 19 May 2005; accepted 13 July 2006

Abstract

In this paper, the porosity of cementitious materials is described in terms of pore size distribution by means of a 3-dimensional overlapping sphere system with polydispersivity in size. On the basis of results established by Lu and Torquato [B. Lu, S. Torquato, Nearest-surface distribution functions for polydispersed particle systems, Phys. Rev. A 45(8) (1992) 5530–5544] and Torquato [S. Torquato, Random Heterogeneous Media: Microstructure and Macroscopic Properties. Springer-Verlag: New York, 2001] providing relations for nearest-neighbor distribution functions, the volume fraction of pores having a radius larger than a prescribed value is explicitly expressed. By adopting an appropriate size distribution function for the sphere system, it is shown that the pore size distribution of cementitious materials as detected for instance by mercury intrusion porosimetry (MIP), which generally points out several pore classes, can be well approached. On the basis of this porosity representation, the evaluation of the capillary pressure in function of the saturation degree is provided. The model is then applied to the simulation of the saturation degree versus relative humidity adsorption curves. The impact of the pore size distribution, the temperature and the thickness of the adsorbed water layer on these parameters are assessed and analyzed for three model materials having different pore characteristics.

Keywords: Polydispersed particle system; Pore size distribution; Modeling; Numerical simulation; Physical properties

1. Introduction

The long-term behavior of cement-based materials is a topic of great concern in many fields of civil engineering, and in particular in the context of nuclear waste storage where these materials could become an attractive option for the construction of disposal engineering barriers, surface and underground structures [3,4]. In this framework, the French Atomic Energy Commission (CEA) has developed research programs aiming at analyzing and characterizing the behavior of such materials subjected to several degradation scenarios. The latter concerns mainly the chemical attacks which are likely to occur in condition of water immersion or flow (as a consequence of ground water), and thermal loading combined with a possible chemical degradation (natural carbonation and steel corrosion essentially) in unsaturated conditions. In this study we focus our attention on the second case where the material is partially saturated. It is well known that for thermo-hydromechanical and atmospheric chemical degradation problems the transport properties of the material and their evolutions are essential for their correct description and modeling. It is also well accepted that these properties are widely related to the microstructure and in particular to the pore network characteristics in terms of pore size and pore length distributions.

In this context an approach providing simple explicit exact relations for describing the porosity in terms of volume and specific surface on the basis of a convenient pore size distribution is proposed. The method permits to estimate some essential parameters regarding mass transfer phenomena such as the capillary pressure $p_c(S_r)$ as a function of the saturation degree S_r, and the saturation degree as a function of relative humidity (or conversely) $S_r(h_r)$. The model is based on the application of nearest-neighbor distribution functions, which are defined as the probability of finding a nearest neighbor at some given distance from a reference point in a system of interacting particles, as proposed by Lu and Torquato [1] and Torquato [2] for a system of 3-dimensional overlapping polydispersed spheres. At first sight, describing the pore structure of cementitious materials by using

---

* Tel.: +33 1 69 08 23 83; fax: +33 1 69 08 84 41.
E-mail address: benoit.bary@cea.fr.

0008-8846/$ - see front matter © 2006 Elsevier Ltd. All rights reserved.
doi:10.1016/j.cemconres.2006.07.001

such sphere systems may appear poorly realistic, because of the complex nature of their microstructure, which exhibits some important connectedness characteristics and correspondingly several pore domains over a wide range of sizes. However, in addition to the derivation of exact results concerning the volume and specific surface for these systems as will be developed in the sequel, some other microstructural descriptors are exactly defined and may be used for improving the pore representation in connection with the corresponding experimental data (in particular the lineal-path function and the chord-length density function [2]), which is not the case for other particle shapes. Also, an important advantage of the overlapping sphere representation for porosity is that it is an actual 3D assemblage with interacting particles, in contrast for example to the very classical representation involving a distribution of cylindrical pores, where it is known that each element is independent. It then leads to the effective existence of menisci (defined as the interfaces separating two fluid phases), which are materialized by the spherical test particles of a given radius inserted in the system for probing it. This aspect is important and justifies the application of the Lu and Torquato approach in the context of unsaturated porous materials. Moreover, the well-defined overlapping sphere assemblage and their explicit analytical surface and volume expressions as a function of the test sphere radius may be used as a benchmark method for evaluating the merits of other empirical or numerical methods describing 3D structure.

Another point of significance regarding the microstructure description is the pore connectivity and the associated percolation properties, in particular when parameters linked to transport properties have to be estimated. Although the pore size domains and their related origin (whether they are intrinsically parts of hydrated products or possibly result from inter-particle spaces) are relatively well defined in the literature concerning cementitious materials, the corresponding pore connectedness lacks generally fine experimental characterization. For example, the percolation threshold for the capillary porosity varies significantly with authors, from a few percent to more than 20%, depending on the experimental procedure or the numerical method adopted (see e.g. [5–7]). From the pore connectivity viewpoint, the polydispersed overlapping sphere system is probably not the most adequate representation of the cementitious material porosity. A system of overlapping ellipsoids would certainly be more realistic and would lead to different results (in particular, it is shown in [8] that the percolation threshold for such systems is as expected strongly influenced by the aspect ratio of these ellipsoids, the maximum value being obtained with the special case of spheres). Moreover, it may be argued that the spatially uncorrelated nature of the particle dispersion in the Lu and Torquato approach makes its use for representing the cementitious material pore network and more particularly its connectivity properties somewhat questionable. Indeed, it is generally accepted that the pore size depends on the spatial location and more precisely on hydration products present at the considered site. Whereas for instance portlandite crystals are non-porous solids, the calcium-silicate-hydrate (C-S-H) phase contains intrinsically an important volume fraction of nanopores (with size varying from the surface to the core, see e.g. [9,10]), which introduces inevitably a certain level of correlation in the particle distribution. It should be noticed that this classical description of the C-S-H phase involving only nanoporosity may be contrasted due to the existence of hollow-shell hydration grains, which can be more or less partly filled, known as Hadley grains [11]. The problem is even more complicated in the case of concrete where the matrix is composed of both volume fraction of aggregates and of hydration products, leading to a much lower value of total porosity, and for this reason this study focuses only on the hydrated cement pastes.

Concerning the use of overlapping ellipsoids system for describing the pore structure, to the author's knowledge, exact and relatively simple analytical results similar to the ones derived by Lu and Torquato for sphere systems are not yet available. Moreover, since the determination of clustering and percolation threshold in the relatively simple case of polydispersed overlapping spheres is far from being trivial [12] (the case of identical spheres is simpler [2,8]), the cases of overlapping ellipsoids and spatially correlated sphere systems appear currently out of reach. For all these reasons, we will consider that the very complex problem of the precise determination of percolation threshold is out of the scope of this paper. This aspect would naturally deserve further investigations, but may be to a certain extent partly circumvented by appropriately taking advantage of some experimental data, in particular those obtained with the very classical test of mercury intrusion porosimetry (MIP). Indeed, it is well established that the MIP results intrinsically include some basic but important connectedness information concerning the porosity, which may consequently alter the results in terms of pore size distribution [2,13–15].

For simplification, it will then be assumed in the following that the whole range porosity of the cement-based materials can be represented by the sphere system with a sufficient accuracy regarding the abovementioned purposes of macroscopic parameter estimation in unsaturated conditions. Correspondingly, the nearest-neighbor distribution functions, which are related to the probability of inserting spheres of given radii in the particle system, are supposed to correctly reproduce the experimental results, especially those obtained with the MIP. Interestingly, other experimental techniques permit to provide a more comprehensive description of porous materials; in particular, a more precise pore size density function can be obtained by applying the so-called B.J.H. method on the adsorption branch of the nitrogen sorption isotherm, this one being unaffected by any percolation effects [16]. In the sequel, it will then be supposed, for the sake of simplicity, that the MIP represents a satisfactory as well as simple mean for characterizing the pore size distribution, keeping in mind that any other technique may alternatively be employed for improving its results. Thus, the objective of this work is clearly not to develop a mercury intrusion simulator, where the hierarchical structure of the porosity exhibited by cementitious materials has to be taken into account in terms of pore length and pore radius correlations, the later having an important impact on the percolation characteristics [14–17].

Once the pore size distribution is experimentally determined, to be successful the method requires a calibration of the size distribution function of the sphere system such that both measured and simulated distributions coincide. The MIP results are generally expressed with the quantity $\psi(r)$ defined as:

$$\psi(r) = \frac{\partial V(r)}{\partial(\ln(r))} = r\frac{\partial V(r)}{\partial r}, \tag{1}$$

where $V(r)$ is the cumulative volume of (accessible) pores having radii $r' > r$; $\psi(r)$ permits indeed to highlight the pore size domains which are dominant in the material. One important purpose of this work is then to explicitly express both functions $V(r)$ and $\psi(r)$ for the sphere system representing the pores, and to relate them to the saturation degree $S_r(r)$. This is the purpose of Sections 2 and 3. Section 4 presents an application of the method to three model materials having different pore size characteristics. Sections 5 and 6 are devoted to the estimation of the capillary pressure curve $p_c(S_r)$ and of the isotherm adsorption curves $S_r(h_r)$, respectively, and an application to the three model materials is provided and commented. Finally, Section 7 concludes this study with some remarks and perspectives.

2. Bases of the model

It is assumed in this study that the porosity of cement-based materials can be described with a system of 3-dimensional overlapping spheres with polydispersivity in size. The definitions and results established in [1,2] concerning void nearest-neighbor distribution function and exclusion probabilities will be used in the following discussions. First of all, the void nearest-surface distribution function $h_v(r)$ is defined such that the quantity $h_v(r)\mathrm{d}r$ corresponds to the probability that at an arbitrary point in the system (which may be in or out of the sphere system), the nearest particle surface is located at a distance comprised between r and $r+\mathrm{d}r$. It is noteworthy to mention that for the continuous polydispersed sphere system, r may range between $-\infty$ and ∞; the negative values of r simply means that the reference point is situated inside the particles. The void exclusion probability function $e_v(r)$ is further defined as the probability of finding a spherical cavity of radius r, centered at an arbitrary point, empty of particle material. This function is related to the nearest-surface distribution function $h_v(r)$ by [1,2]:

$$e_v(r) = 1 - \int_{-\infty}^{r} h_v(x)\mathrm{d}x \tag{2}$$

It follows from Eq. (2) that:

$$h_v(r) = -\frac{\partial e_v(r)}{\partial r} \tag{3}$$

Based on exact series expansions of $h_v(r)$ and $e_v(r)$ for a system of overlapping (spatially uncorrelated) spheres with continuous distribution in radius R characterized by a normalized probability density function $f(R)$, Lu and Torquato [1] have established the following results:

$$\begin{aligned} e_v(r) &= \exp(-\rho\langle v(r+R)H(r+R)\rangle) \\ h_v(r) &= \rho\langle s(r+R)H(r+R)\rangle e_v(r) \end{aligned} \tag{4}$$

in which $v(R)$ and $s(R)$ are the volume and surface area of a sphere with radius R, respectively:

$$v(R) = \frac{4}{3}\pi R^3, \qquad s(R) = 4\pi R^2 \tag{5}$$

In Eq. (4), H is the Heaviside step function ensuring that the argument $(r+R)$ remains positive; ρ is the total number density; $\langle X(R)\rangle$ defines the average of any function $X(R)$ as:

$$\langle X(R)\rangle = \int_0^\infty X(R)f(R)\mathrm{d}R \tag{6}$$

Relations (4) are valid for both negative and positive r. In the ensuing developments, these expressions will be employed for negative values of r, since we are mainly interested in characterizing the porosity phase, which is assumed here to be the particle phase. It is worth noting that the porosity phase may be as well defined as the phase being outside the particle phase; however for a better characterization and experimental identification of the pore size distribution it seems more convenient to understand a particle as part of a pore. In this case, $e_v(r)$ is interpreted as the probability that there is no particle material which penetrates the reference point with a distance greater than $-r$, whereas $h_v(r)$ is the probability density corresponding to the occurrence of finding the nearest surface situated at a distance of $-r$ from a reference point in the particle phase [1]. Accordingly, $e_v(r)$ represents the expected fraction of space available to a test particle of radius $-r$ when inserted in the particle phase [2]. For the practical applications on cementitious materials presented hereafter, $e_v(r)$ is of particular importance. Fig. 1 shows an illustrative and simple example which permits to intuitively appreciate this quantity in the case of a 2D polydispersed sphere (a more appropriate term would be disk in this case) system when $r<0$. In this example the particle phase is composed of several overlapping spheres, the biggest having the radius r_1, then followed by a sphere with radius $r_2<r_1$ and one with radius $r_3<r_2$; all other sphere radii r_i are such that $r_i<r_3$. It is of course impossible to insert a test sphere with radius $\delta>r_1$ in this particle system, and the associated probability of finding a spherical cavity of radius $\delta>r_1$ is zero. Thus, it is clear from the above definition of $e_v(r)$ that $e_v(r)=1$ for $r<-r_1$. Likewise, the biggest test sphere that can be inserted in the system has the radius r_1 and can be uniquely placed at the exact location of the particle with radius r_1. Correspondingly, the quantity $1-e_v(-r_1)$ represents the volume of this test sphere. If we try now to insert a test sphere of radius r_3 in the system, we immediately remark that the volume which can be occupied by this test sphere is exactly the cavity formed by the three biggest particles, which does not correspond to the one of the three particles considered separately since in our example

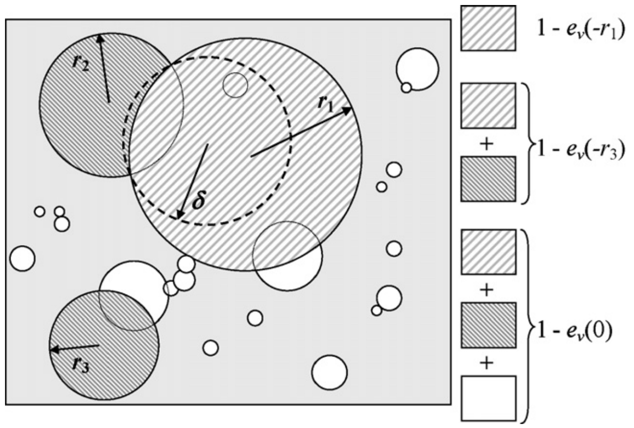

Fig. 1. 2D schematic illustration of a system of polydispersed overlapping spherical particles representing pore space ($r_1>r_2>r_3$). The particle volume that can be occupied by test spheres with radius r_1, r_2 and 0 are indicated, and δ is such that $r_1>\delta>r_2$.

they overlap; this volume is given by $1-e_v(-r_3)$. Note that for intermediate test sphere radii δ such that for example $r_1>\delta>r_2$, the cavity volume accessible to this test sphere varies continuously due to particle interpenetration. Indeed, in this case the test sphere is allowed to progressively penetrate further in the smallest particle as its radius decreases. This is illustrated in Fig. 1 where a test sphere with radius δ represented in dotted line is inserted in the overlapping zone of the two biggest particles. It then appears clearly that the volume which can be occupied by this sphere becomes gradually larger than the volume of the bigger of the two particles.

Interestingly, a similar approach for polydispersed hard-sphere systems leading to approximate solutions for the void exclusion probability $e_v(r)$ has been used in the context of cement-based materials in [18,19].

The definitions of $h_v(r)$ and $e_v(r)$ further imply the equalities:

$$e_v(0) = \phi_2, \qquad h_v(0) = \phi_2 S \tag{7}$$

where S is the specific surface of the sphere system and ϕ_2 is its complementary volume fraction (the volume fraction of the particle phase is then $\phi_1=1-\phi_2$). The pore size probability density function $P(\delta)$ and the corresponding complementary cumulative distribution function $F(\delta)$ are related to the nearest-surface functions via the expressions [2]:

$$P(\delta) = \frac{h_v(\delta)}{\phi_1}, \qquad F(\delta) = \frac{e_v(\delta)}{\phi_1}\ , \delta \geq 0 \tag{8}$$

Recall that, as already mentioned in the Introduction, $P(\delta)$ and $F(\delta)$ do not integrate some pore connectivity information which are intrinsically included in experimental results involving fluid intrusion, such as MIP [13].

Before expressing in details $h_v(r)$ and $e_v(r)$ for some choices of size distribution function $f(R)$, it is important to relate the function $e_v(r)$ and the degree of saturation $S_r(\delta)$ for a given radius of pore δ. The function $S_r(\delta)$ is defined as the complementary volume fraction of the total porosity which can be filled by inserting spherical particles of radii $r \geq \delta$. It is then implicitly supposed that all the pores having radius $r \geq \delta$ are empty of free water (to be distinguished with the adsorbed water layer on pore surface, which will be introduced in the model in Section 4), whereas the pores with radius $r<\delta$ are totally filled with the liquid. In this condition the material is said to be macroscopically partially saturated. We further introduce the volume fraction of material, denoted as $\phi_1(-\delta)$, filled by inserting spheres of radii $r \geq \delta$ in the particle phase. Thus, with these definitions it is immediate that:

$$\phi_1(-\delta) = V(\delta) = 1 - e_v(-\delta) \quad \text{and}$$
$$S_r(\delta) = \frac{e_v(-\delta) - \left(1-\phi_1^0\right)}{\phi_1^0} \quad (\text{for } \delta>0) \tag{9}$$

where $\phi_1^0 = \phi_1(0)$. Relation (9) plays a key role in the ensuing developments and applications. Fig. 2 illustrates on the schematic pore space representation of Fig. 1 the volume fractions of particles occupied by water and air respectively, and the corresponding shape of the gaseous–liquid interface, for the case $r_2<\delta<r_1$. As explained in the case of Fig. 1, the volume that can occupy the test sphere of radius δ inserted in the system is different from the one of the sphere with radius r_1, due to particle overlapping. Indeed, menisci materializing the gaseous–liquid interface appear when introducing such test spheres in the zones where the particles interpenetrate, as represented by dotted lines in Fig. 2. The cavity then formed by the space accessible to the test sphere, which is $\phi_1(-\delta) = 1-e_v(-\delta)$, is supposed to be filled with air, whereas the remaining complementary volume of particles ($\phi_1(0) - \phi_1(-\delta)$) is assumed to be filled by water. Accordingly, $S_r(\delta)$ is defined in Eq. (9) by the ratio between this volume fraction of water and the total volume fraction of particles ϕ_1^0. Two important remarks have to be made concerning the establishment of Eq. (9). Firstly, the assumption that the interface separating the gaseous and liquid phases present in the porosity is composed of portions of perfectly spherical interfaces is intrinsically adopted, together with the fact that the contact angle of the interface with the pore wall is zero. These hypotheses follow from the spherical form of

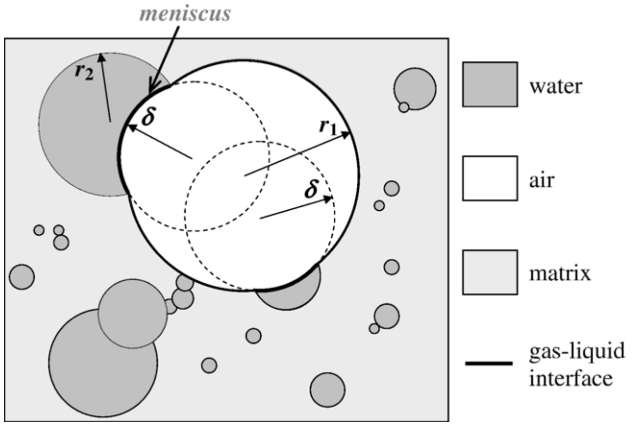

Fig. 2. 2D schematic illustration of a partially saturated spherical particle system; $S_r(\delta)$ is the volume fraction of water over the volume fraction of particles (here δ is such that $r_2<\delta<r_1$).

the 'test' particles. Secondly, as already mentioned, the condition concerning the fraction of the porosity filled by insertion of these spherical 'test' particles is supposed to be satisfied everywhere in the material, whatever the connectedness of the porosity network. It is assumed that this situation would be obtained in the case of imbibition of a material initially totally free of liquid, after a sufficient duration of the process (achieved when the mass change is stabilized).

With relation (9), the expression of $\psi(\delta)$ defined in Eq. (1) can be recast as:

$$\psi(\delta) = \delta\frac{\partial V(\delta)}{\partial \delta} = -\delta\frac{\partial e_{\mathrm{v}}(-\delta)}{\partial \delta} = \delta h_{\mathrm{v}}(-\delta) \tag{10}$$

It is then noted that $\psi(\delta)$ expresses simply via the function h_{v}.

3. Multiple pore size classes

It is well known that cement pastes (and consequently mortars and concretes) usually exhibit several pore size classes. Besides, a distinction is generally made between the porosity of the hydration products (due essentially to C-S-H phase), and the porosity resulting from cement inter-particle spaces, initially containing water, and which are not totally filled by hydrated products. The latter is denoted as capillary porosity and is strongly dependant on the water over cement ratio (w/c); its characteristic pore size ranges from about 100 μm to several mm. Likewise, the porosity of C-S-H is usually divided into two families, namely microporosity (typical diameter of 20–30 nm) and nanoporosity (typical diameter of 2 to 4 nm), which are associated with two different kinds of C-S-H (inner and outer, or equivalently high density and low density C-S-H), resulting from whether the formation process is restricted or not by space, according to many authors (see e.g. [14,20]). It is then of interest to apply the results exposed in the previous section to the case of cementitious materials having N pore size classes ($N>1$). It is proposed to naturally introduce these N classes in the size distribution function $f(R)$ by making use of a sufficient number of normalized size distribution functions $f_i(R)$, each of them characterizing one class of pores. Then $f(R)$ is defined as:

$$f(R) = \xi_i f_i(R), \quad \sum_{i=1}^{N} \xi_i = 1 \tag{11}$$

The coefficients ξ_i are positive scalars and have to satisfy the constraint (11) in order to maintain the normalization of $f(R)$. Denoting $\bar{R}$ and $\bar{R}_i$ the average radii of the whole particle system and of the class i, respectively, as:

$$\bar{R} = \langle R\rangle,\ \bar{R}_i = \langle R\rangle_i \text{ with } \langle X(R)\rangle_i = \int_0^{\infty} X(R) f_i(R)\,\mathrm{d}R \tag{12}$$

the following results are obtained:

$$\overline{R}^{n} = \xi_i \overline{R}_i^{n},\ \ \phi_2 = \prod_{j=1}^{N} \phi_{2j}^{\xi_j}, \phi_{2i} = \phi_{2j}^{(\bar{R}_i/\bar{R}_j)^3} \ \text{(no sum)} \tag{13}$$

where $\phi_{2i} = e_{\mathrm{v}i}(0) = \exp(-\rho\langle v(R)\rangle_i)$, and n is an integer. The expressions of $h_{\mathrm{v}}(r)$ and $e_{\mathrm{v}}(r)$ become simply:

$$\begin{aligned} e_{\mathrm{v}}(r) &= \exp\left(-\rho\left(\xi_i\langle v(r+R)H(r+R)\rangle_i\right)\right) \\ h_{\mathrm{v}}(r) &= \rho\left(\xi_i\langle s(r+R)H(r+R)\rangle_i\right)e_{\mathrm{v}}(r) \end{aligned} \quad \text{(with sum)} \tag{14}$$

Among the large diversity of size distribution functions proposed in the literature, we chose the Schulz distribution defined as (see e.g. [2]):

$$f_i(R) = \frac{1}{\Gamma(m_i+1)}\left(\frac{m_i+1}{\bar{R}_i}\right)^{m_i+1} R^{m_i} \exp\left(-\frac{m_i+1}{\bar{R}_i}R\right) \tag{15}$$

where $\Gamma(x)$ is the Gamma function. When the positive parameter m_i is limited to integer values, we have $\Gamma(m_i+1) = m_i!$; in the sequel this restriction will be adopted for the sake of simplicity. The distribution becomes sharper when m_i increases, and the limit case $m_i \rightarrow \infty$ corresponds to a monodisperse distribution. In Fig. 3 the Shultz size distributions for several values of m_i are depicted.

The development of expression (14) for negative values of r requires the terms involving $H(r+R)$ to be precise; we then have:

$$\langle X(r+R)H(r+R)\rangle_i = \int_{-r}^{\infty} X(r+R) f_i(R)\,\mathrm{d}R \ \ (\text{for } r<0) \tag{16}$$

Moreover, since the nth moment $\langle R^n H(r+R)\rangle_i$ of the distribution $f_i(R)$ enters in Eq. (14) for $n \leq 3$, it is useful to express it for the particular choice of the Schultz distribution (15). Using identity (16), $\langle R^n H(r+R)\rangle_i$ takes the explicit following form:

$$\begin{aligned} &\langle R^n H(r+R)\rangle_i \\ &= \left[\sum_{j=0}^{m_i+n} \frac{(m_i+n)!}{(m_i+n-j)!}(-r)^{m_i+n-j}\left(\frac{\bar{R}_i}{m_i+1}\right)^{j}\right]\left(\frac{m_i+1}{\bar{R}_i}\right)^{m_i}\frac{1}{m_i!}\exp\left(\frac{m_i+1}{\bar{R}_i}r\right) \end{aligned} \tag{17}$$

Making use of Eq. (17), the quantities $\langle v(r+R)H(r+R)\rangle_i$ and $\langle s(r+R)H(r+R)\rangle_i$ can be also explicitly expressed in the following compact form:

$$\begin{aligned} &\langle v(r+R)H(r+R)\rangle_i \\ &= \frac{4\pi}{3}\left[\sum_{j=3}^{m_i+3} \frac{j(j-1)(j-2)}{(m_i+3-j)!}\left(\frac{m_i+1}{\bar{R}_i}\right)^{m_i-j}(-r)^{m_i+3-j}\right]\exp\left(\frac{m_i+1}{\bar{R}_i}r\right) \end{aligned} \tag{18}$$

$$\begin{aligned} &\langle s(r+R)H(r+R)\rangle_i \\ &= 4\pi\left[\sum_{j=2}^{m_i+2} \frac{j(j-1)}{(m_i+2-j)!}\left(\frac{m_i+1}{\bar{R}_i}\right)^{m_i-j}(-r)^{m_i+2-j}\right]\exp\left(\frac{m_i+1}{\bar{R}_i}r\right) \end{aligned} \tag{19}$$

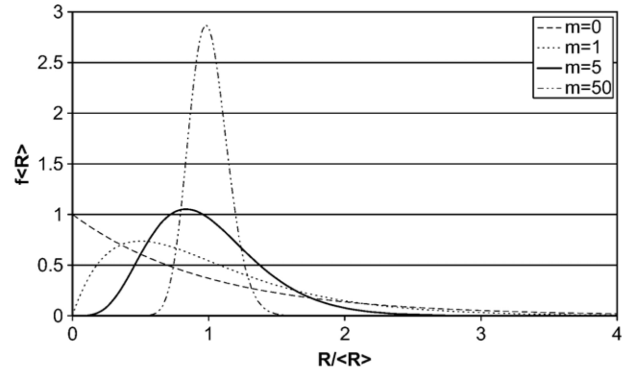

Fig. 3. Shultz size distribution function for several values of m, normalized with respect to the average radius of the particle system $\langle R\rangle$.

Relations (18) and (19) are essential in the ensuing development because they relate directly the porosity and saturation degree as defined by Eq. (9) to a pore size corresponding to the limit of fluid intrusion, via Eq. (14). In the following sections several applications of these results for two values of m_i are given.

4. Application to cementitious materials

It will be shown in this section that with appropriate choices of the size distribution functions $f_i(R)$ (that is, with some suitable values for the coefficients m_i and the average radii $\overline{R}_i$), the numerical results agree relatively well both qualitatively and quantitatively with experimental ones obtained on cementitious materials in terms of $V(\delta)$ and $\psi(\delta)$ in function of the radius of accessible pore. For the sake of simplicity, in the ensuing developments the same value of m_i will be used for all pore classes, and then $m_i = m$. Moreover, to avoid some confusion between the radius involved in Eq. (14) and the one appearing in Eq. (10), from now on the positive variable $\delta = -r$ will be systematically employed (recall that h_v and e_v are defined with negative values of radius for characterizing the particle phase). With these conditions, we can express $e_\mathrm{v}(-\delta)$ and $h_\mathrm{v}(-\delta)$ for any given values of m as a function of $\overline{R}_i$, by means of Eq. (14). For the particular cases of $m=1$ and $m=5$ we get:

$$\begin{cases} e_{\mathrm{v}m=1}(-\delta) = \exp\left[-\rho\dfrac{4\pi}{3}\xi_i\left(\dfrac{3}{2}\delta\overline{R}_i^2 + 3\overline{R}_i^3\right)\exp\left(-\dfrac{2\delta}{\overline{R}_i}\right)\right] \\ \qquad\qquad\qquad\qquad\qquad\qquad\qquad\qquad\qquad\qquad \text{(with sum)} \\ h_{\mathrm{v}m=1}(-\delta) = 4\rho\pi\left[\xi_i\left(\delta\overline{R}_i + \dfrac{3}{2}\overline{R}_i^2\right)\exp\left(-\dfrac{2\delta}{\overline{R}_i}\right)\right]e_{\mathrm{v}m=1}(-\delta) \end{cases} \tag{20}$$

$$\begin{cases} e_{\mathrm{v}m=5}(-\delta) = \exp\left[-\rho\dfrac{4\pi}{3}\xi_i\begin{pmatrix}\dfrac{9\delta^5}{5\overline{R}_i^2} + 6\dfrac{\delta^4}{\overline{R}_i} + 10\delta^3 \\ +10\overline{R}_i\delta^2 + \dfrac{35}{6}\delta\overline{R}_i^2 + \dfrac{14}{9}\overline{R}_i^3\end{pmatrix}\exp\left(-\dfrac{6\delta}{\overline{R}_i}\right)\right] \\ h_{\mathrm{v}m=5}(-\delta) = 4\rho\pi\left[\xi_i\begin{pmatrix}\dfrac{18\delta^5}{5\overline{R}_i^3} + 9\dfrac{\delta^4}{\overline{R}_i^2} + 12\dfrac{\delta^3}{\overline{R}_i} \\ +10\delta^2 + 5\delta\overline{R}_i + \dfrac{7}{6}\overline{R}_i^2\end{pmatrix}\exp\left(-\dfrac{6\delta}{\overline{R}_i}\right)\right]e_{\mathrm{v}m=5}(-\delta) \end{cases} \tag{21}$$

For a practical use of these results regarding an application to cementitious materials, $2N$ parameters have to be identified or adjusted: $\overline{R}_i$, ξ_i, and ρ (recall constraint (11)). It is shown that the values of $\overline{R}_i$ and ξ_i can be evaluated from experimental results via the cumulative volume $V(\delta)$ and $\psi(\delta)$ curves. Indeed, referring to $\psi(\delta)$ for calibrating the position of the peaks characterizing the pore size classes, these peak positions are obtained by solving the set of equation:

$$\begin{aligned} \frac{\partial\psi(\delta)}{\partial\delta} &= \frac{\partial(\delta h_\mathrm{v}(-\delta))}{\partial\delta} = 0 \\ &\equiv -\delta\left(\frac{\partial s_1(-\delta)}{\partial\delta} - \rho s_1^2(-\delta)\right) - s_1(-\delta) = 0, \quad \frac{\partial^2\psi(\delta)}{\partial\delta^2} < 0 \end{aligned} \tag{22}$$

with $s_1(-\delta) = \langle s(-\delta+R)H(-\delta+R)\rangle$. These equations do not appear to have explicit roots, even for a unique class of pores, and they will then be solved numerically; it is noteworthy that these roots are a priori different from the $\overline{R}_i$ introduced in $f_i(R)$. Moreover, the cumulative volume $V(\delta)$ experimentally obtained permits to identity the parameters ξ_i: $i-1$ experimental values of $V(\delta)$ are then required for different δ.

From now on, it is assumed that the different pore classes are well separated, with at least one order of magnitude between the average radii of two consecutive classes. This hypothesis, which is in relatively good agreement with cementitious materials, allows to estimate both $e_\mathrm{v}(-\delta)$ and $h_\mathrm{v}(-\delta)$ for $\delta = \overline{R}_i$. Indeed, denoting $\overline{R}_N = \mathrm{Sup}\{\overline{R}_i\}$ and $\overline{R}_1 = \mathrm{Inf}\{\overline{R}_i\}$, $e_\mathrm{v}(-\overline{R}_i)$ and $h_\mathrm{v}(-\overline{R}_i)$ can be evaluated by neglecting the terms involving $\overline{R}_j$ such that $j = \{1; i-1\}$ in Eqs. (20) and (21), with the approximation that $\exp(-a\overline{R}_i/\overline{R}_j) \approx 0$ (with $a=2$ when $m=1$ and $a=6$ when $m=5$). This simplification is applicable under the condition that the identification of $\overline{R}_i$ and ξ_i is performed from the greater average radius towards the lower, i.e. from $\overline{R}_N$ to $\overline{R}_1$.

Moreover, an estimate of ρ can be furnished by considering that ϕ_{21}, according to Eq. (13), is such that $\phi_{21} \gg \phi_{2j}$, $\forall_j$, due to the assumption that $\overline{R}_j \gg \overline{R}_1$. In this condition it follows that $\xi_1 \gg \xi_j$, and therefore $\xi_1 \approx 1$ as a result of Eq. (11). The total number of particles ρ can then be estimated via:

$$\rho_{m=1} \approx -\frac{\ln(1-\phi_{21})}{4\pi\overline{R}_1^3}, \quad \rho_{m=5} \approx -\frac{27\ln(1-\phi_{21})}{56\pi\overline{R}_1^3} \tag{23}$$

The expressions given in Eq. (23) require the knowledge of both ϕ_{21} and $\overline{R}_1$, which is a limitation of their applicability; however they improve and facilitate the numerical identification of $\overline{R}_i$ and ξ_i.

An application of the preceding results to the case of three 'model' materials having different characteristics but exhibiting only two pore classes for the sake of simplicity, and for the two values $m=1$ and $m=5$ is now presented. The motivation for this comparative study is twofold. First, it permits to illustrate and evaluate the global capacities of the proposed method. Second, it allows estimating and analyzing the effects of the microstructure information in terms of pore size distribution on some key factors regarding the transfer phenomena in unsaturated conditions, as $p_c(S_r)$ and $S_r(h_r)$ (see the next two sections). Accordingly, the material characteristics are chosen so that the pore size distributions exhibit significant differences regarding their two main features, namely the porosity and the pore size classes values, with the condition of remaining representative of a real microstructure (that is, comparable with MIP results). The parameters used in the numerical simulations are reported in Table 1 and are adapted from the case of a CEM I cement paste with water to cement ratio = 0.43 in [21] for Material 1 in terms of $\psi(\delta)$ (main pore domains) and $V(\delta)$. Material 3 corresponds to Material 1 which has undergone an accelerated chemical degradation in saturated conditions [21]; consequently, the dissolution and decalcification of the main hydrated products have led to an increase of the total porosity combined to a significant displacement toward greater pore sizes of the pore classes. It should be noticed that pore sizes smaller than 2–3 nm can generally not be reached with the MIP technique, and the data indicated in the table are extracted in this case from measurements obtained with the B.J.H. method [22]. The porosity ϕ_{21} for Material 1 has been adjusted for both values of m such that the cumulative volume fraction $V(\delta)$ is equal to the experimental value of 0.045 for $\delta = \delta_2$. Material 2 is similar to Material 1 regarding the peak positions for the two pore classes, but has a lower total porosity; it is moreover subjected to the constraint $V(\delta = 7 \times 10^{-9}) = 0.05$. This permits to evaluate the repercussions of the porosity on the results, and in particular the porous space repartition between the two pore domains, independently of the peak position.

The characteristics of the three model materials in terms of $h_v(-\delta)$, $\psi(\delta)$ and $V(\delta)$ functions are depicted in Figs. 4, 5 and 6, respectively. Recall that $\psi(\delta)$ and $V(\delta)$ can be directly related to MIP results: ψ indicates the main pore classes and V measures the cumulative volume of intruded fluid as a function of pore access radius. The evolutions of these functions for Material 3 are as expected strongly different from those of the two other materials, which are comparatively closer. Since the case with $m = 5$ corresponds to a sharper pore size distribution for both pore classes, the variations in magnitude for higher and lower peaks in the $\psi(\delta)$ curve appear to be larger than for the case with $m = 1$, for which the size distribution is broader. On the opposite, as the main characteristics of the pore distribution are constrained to be quite similar in terms of porosity and peak location for the two cases, the $e_v(-\delta)$ functions, and then $V(\delta)$, are necessarily comparable.

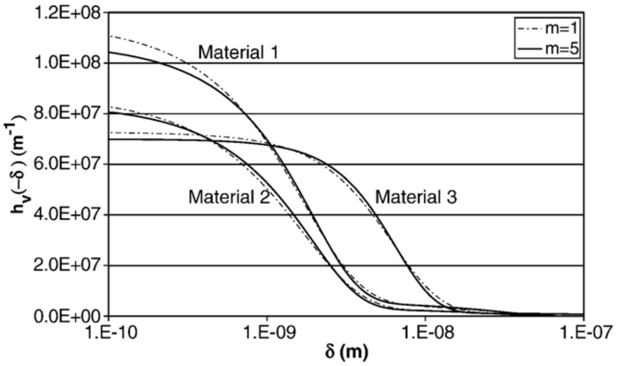

Fig. 4. Evolutions of $h_v(-\delta)$ as a function of δ for the three model materials and for $m = 1$ and $m = 5$.

It should be noted that the specific surface of the pore space (interface area per unit volume) given by $h_v(0)$ (see [1,2] for further details) underestimates in this case the typical values experimentally obtained for cement pastes, which are over 100 m^2/g depending on the drying procedure performed on the specimen before testing [22,9]. Indeed, the mass density of this material being about 3 g/cm^3, the specific surface estimated by $h_v(0)$ for Material 1 is comprised between 35 and 40 m^2/g. The reason of this difference may be explained by the fact that the bimodal size distribution as retained for describing the pore structure, due to its simplicity, does not take well into account the smallest pores which in practice are attributed to the C-S-H. These pores appear to exhibit an important specific surface but comparatively do not contribute significantly to the total porosity [9].

To conclude this section, it is noticed that the obtained numerical results for Materials 1 and 3 in terms of $\psi(\delta)$ and $V(\delta)$ evolutions agree relatively well with the MIP experimental data presented in [21], in particular in the case with $m = 5$, which means that the pore size distribution for these materials is rather tightened. It is also remarked that the values of $\overline{R}_i$ are systematically greater in the case of $m = 5$, and in contrast the total number of particles ρ is lower.

5. Evaluation of the capillary pressure curve

In this section the results previously established are applied to the estimation of the evolutions of the capillary pressure p_c as a function of the saturation degree S_r. The capillary pressure is

Table 1
Characteristics of the pore classes for the three model materials

	Material 1		Material 2		Material 3	
	$m=1$	$m=5$	$m=1$	$m=5$	$m=1$	$m=5$
ϕ_1	0.30	0.30	0.20	0.20	0.60	0.60
δ_1 ($\times 10^{-9}$ m)	1.6	1.6	1.6	1.6	5	5
δ_2 ($\times 10^{-9}$ m)	22	22	22	22	150	150
$\overline{R}_1$ ($\times 10^{-9}$ m)	2.092	3.261	2.171	3.36	6.011	9.15
$\overline{R}_2$ ($\times 10^{-9}$ m)	32.27	49.38	32.1	49.28	211	313
ξ_1	0.99984	0.9986	0.99986	0.99985	0.99999	0.99999
ξ_2	0.000165	0.0014	1.432×10^{-4}	1.448×10^{-4}	6.483×10^{-6}	7.623×10^{-6}
ρ ($\times 10^{23}$)	19.33	9.499	11.86	6.144	2.512	1.413

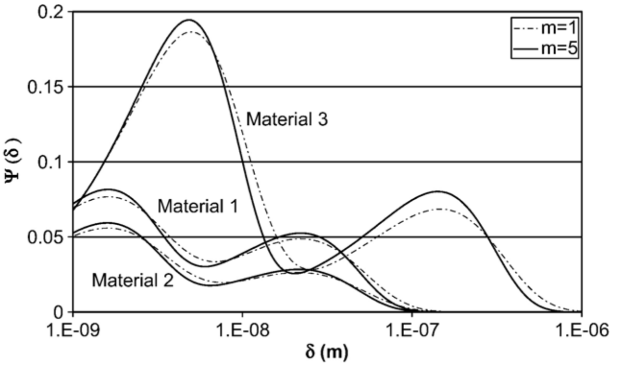

Fig. 5. Evolutions of $\psi(\delta)$ as a function of δ for the three model materials and for $m=1$ and $m=5$.

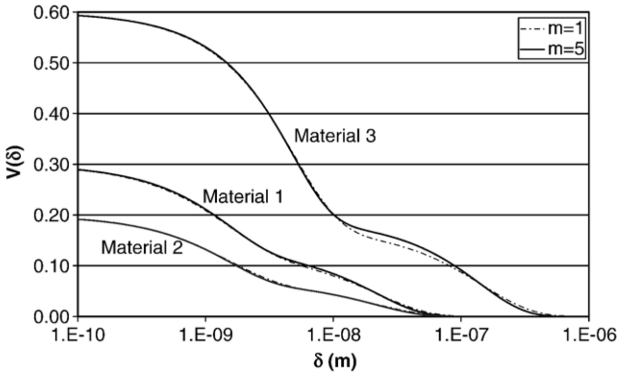

Fig. 6. Evolutions of $V(\delta)$ as a function of δ for the three model materials and for $m=1$ and $m=5$.

defined as the difference between the pressure of the gaseous phase and the liquid one, these two fluid phases being separated by a non-planar interface. The $p_c(S_r)$ function is of great importance in many practical problems dealing with mass transfer in partially saturated porous media; in particular, it enters in most of the modeling involving water transfers in cementitious materials, such as thermo-hydromechanical problems, and degradation due to external aggressive agents (see e.g. [23–27]). The major reason is that this function, which is generally experimentally determined, integrates at the macroscopic scale a high level of microstructure information in terms of pore size distribution and connectedness. Correspondingly, it is deeply related to the material microstructure and then evolves when this latter changes, as a consequence for example of heat induced damage or chemical degradations.

To illustrate the influence of the microstructure described in terms of its pore size distribution on the capillary pressure curve, the three model materials defined in the previous section are analyzed for the two values $m=1$ and $m=5$. In the ensuing discussion, it will be supposed that the concept of capillary pressure at macroscopic scale is applicable, keeping in mind that for the lower pore radii (and then saturation degree) it is highly questionable; indeed in these conditions the behavior of the gas–liquid interface is essentially governed by the adsorbed water film, the meniscus becoming very small and then having lesser effects (see e.g. [28]). The basic equation relating the capillary pressure and the pore radius is due to Laplace and takes the form:

$$p_c = \frac{2\sigma_{gl}\cos\theta}{\overline{r}} \tag{24}$$

where σ_{gl} is the gas–liquid interfacial tension, θ is the contact angle between the gas–liquid interface and the solid phase, and $\overline{r}$ is the mean curvature radius of the gas–liquid interface. In the case of a spherical meniscus of radius δ we then have $\overline{r}=\delta$. It is generally assumed for simplicity that $\theta=0$ for cementitious materials (see e.g. [29]), and the preceding relation then becomes:

$$p_c = \frac{2\sigma_{gl}}{\delta} \tag{25}$$

The saturation degree S_r is defined as a function of the pore radius δ, which is equal to the radius of the test sphere probing the particle phase, in Eq. (9). However, this relation does not yet include the effects of the adsorbed water layer on the pore surface for pores having radius $\delta'>\delta$ which are empty of free water. The thickness t of this layer depends on the partial pressure p_v of the water vapour present in the gaseous phase, or equivalently on the relative humidity h_r defined as $h_r=p_v/p_{vs}$, where p_{vs} is the saturation pressure of vapour. It is proposed to adopt the following expression for t:

$$t = \left(\frac{2.4}{0.85+(-\log h_r)^{0.57}}\right)^{2.785} \quad (\text{in Å}) \tag{26}$$

This relation is adapted from Harkins and Jura for nitrogen (see e.g. [16]), and is plotted together with the experimental results from Hagymassy et al. [30] in Fig. 7. The expression of S_r is then modified as follows:

$$S_r(\delta) = \frac{e_v(-\delta-t)-\left(1-\phi_1^0\right)}{\phi_1^0} \tag{27}$$

Indeed, due to the spherical form of the particles, and with the hypothesis of spherical meniscus for the gas–liquid interface (corresponding to the test sphere surface), the effect of the adsorbed layer can be simply taken into account by withdrawing its thickness t to the radius of the test sphere δ. Equivalently, this effect is to be interpreted as a reduction of the radius for all

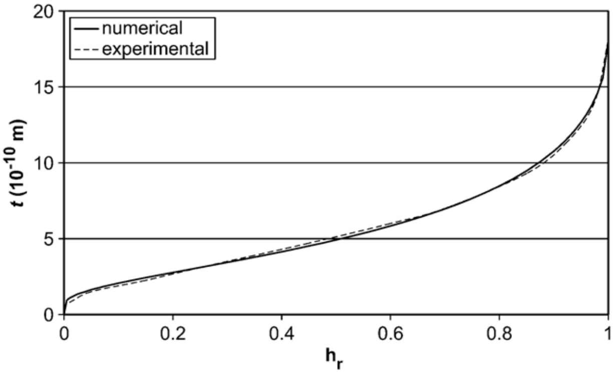

Fig. 7. Numerical and experimental [30] evolutions of the adsorbed layer thickness t versus the relative humidity h_r.

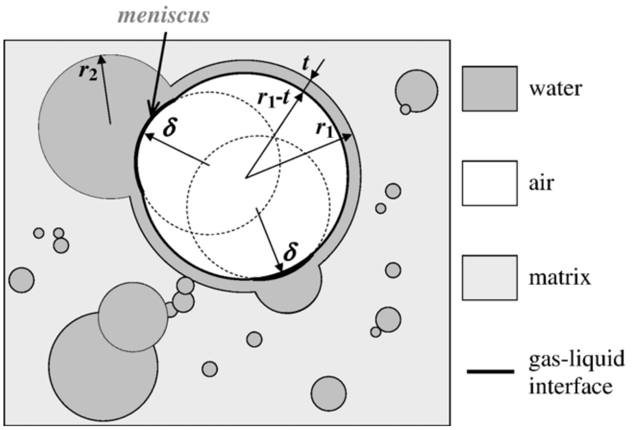

Fig. 8. 2D schematic illustration of a partially saturated spherical particle system with the adsorbed water layer of thickness t; $S_r(\delta)$ is the volume fraction of water over the volume fraction of particles (δ is such that $r_2 < \delta < r_1$).

particles (more precisely, for all particles with radius greater than t) by t. Fig. 8 illustrates schematically the consequences of the adsorbed layer thickness t on the saturation degree S_r, in comparison with the case of Fig. 2 where it is not taken into account. To make the comparison easier, test spheres of radius δ are again represented in Fig. 8 for characterizing menisci which materialize the interface between the free water and the gaseous phase. It is clear from Fig. 8 that the radius of the meniscus involved in the expression giving the capillary pressure is δ, whereas the volume accessible to the test sphere is obtained by reducing the particle radius by t.

We adopt for σ_{gl} the expression proposed in [31] as follows:

$$\sigma_{gl} = 0.1558\left(1 - \frac{T}{647.1}\right)^{1.26} \quad (\text{in N/m}) \tag{28}$$

where T is the absolute temperature. To close the system of equations, it is necessary to relate p_c and h_r: this is done by making use of the well-known Kelvin's law which takes the form:

$$p_c = -\rho_l \frac{RT}{M_v} \ln h_r \tag{29}$$

where M_v is the molar mass of water vapour and R the gas constant; ρ_l is the density of the liquid water which is assumed to follow the expression given in [32] as:

$$\rho_l = 314.4 + 685.6\left[1 - \left(\frac{T - 273.15}{374.14}\right)^{\frac{1}{0.55}}\right]^{0.55} \quad \left(\text{in kg/m}^3\right) \tag{30}$$

The set of Eqs. (25)–(26) and (28)–(30) provides in an implicit form the variations of the capillary pressure p_c as a function of the pore radius δ, via the calculation of the relative humidity h_r and of the thickness of the adsorbed water layer t. Since the saturation degree S_r is also related to δ by Eq. (27), Eqs. (25)–(30) then permit to obtain computationally the $p_c(S_r)$ curves.

The numerical $p_c(S_r)$ curves for the three model materials and the two cases $m=1$ and $m=5$ are shown in Fig. 9. Not surprisingly, significant differences between the three materials, especially between Material 3 and the two others, can be observed. Materials 1 and 2 curves are close for saturation degrees higher than 0.85; for lower saturation levels, the curves can be approximately deduced by a translation toward higher values of p_c for Material 2. This observation can be attributed to the fact that Material 2 has the same pore classes as Material 1 but with a different repartition of the porosity between them. This result illustrates the importance of the pore class porosity with respect to the total porosity on the capillary pressure curves. It can be noticed that the influence domain of each pore class appears clearly on the numerical results; in particular, the limit between the two pore classes, which can be materialized by the lower peaks on the $\psi(\delta)$ curves, corresponds to the zone with negative curvature radii on the capillary pressure curves.

The results obtained for Material 3 highlight the importance of the pore size distribution on the $p_c(S_r)$ curve. Indeed, in this case the capillary pressure remains very low for saturation degrees higher than 0.7, due to the relatively large pores drained in this saturation domain (average radius centered around 150×10^{-9} m). Moreover, for all S_r, the pressures predicted in the cases of Materials 1 and 2 are significantly greater than for Material 3. Again, this is explained by the fact that the major part of the porosity volume fraction is obtained for much larger pores in the case of Material 3. The proposed model then provides a quantitative mean to evaluate the dependence of the pore size distribution upon the capillary pressure curve. From the numerical simulations, it is clear that this strong dependence cannot be ignored and should be carefully evaluated, in particular when the microstructure of the material evolves, as a consequence for example of chemical degradation.

To assess the impact of the thickness t of the adsorbed water layer on the preceding results, it is presented in Fig. 10 the evolutions of the capillary pressure curve for Material 1 in the following configurations: t is included in the calculations for both p_c and S_r (a), t is only included in the expression of S_r (b), and t is considered to be 0 (c). The configuration (b) corresponds to the model as presented in this paper, whereas (a) is a virtual situation in which δ is replaced by $\delta - t$ in the Laplace equation, in other words the capillary pressure is expressed by $p_c = 2\sigma_{gl}/(\delta - t)$. The effects of t appear then to be

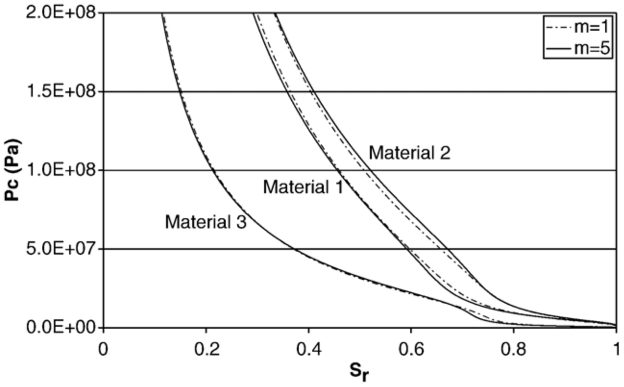

Fig. 9. Evolutions of $p_c(S_r)$ for the three model materials and the two cases $m=1$ and $m=5$.

significant for this material especially for saturation degree lower than 0.7–0.8, that is, for smaller pore radii. In fact, it appears that t may be neglected for high values of δ (corresponding approximately to $S_r > 0.8$), whereas its impact is proportionally more important for lower δ. In other words, t is all the more negligible than it is 'small' relative to δ.

To conclude this section, we propose to evaluate the consequences of a moderate increase of temperature on the capillary pressure curve. It will be assumed that Eq. (26) relating the adsorbed water layer thickness and the relative humidity is not changed by this temperature evolution [22]. However it is well known that, since p_{vs} is strongly dependent on the temperature, h_r necessarily will be affected by this change. In this condition Eqs. (25)–(30) are able to provide the $p_c(S_r)$ curves as a function of the temperature, or $p_c(S_r, T)$. The results for Material 1 with $m=5$ are presented in Fig. 11 for the following values of temperature: 20, 40, 70 and 100 °C. It is observed that the differences between the curves become significant for saturation degree values lower than 0.6–0.7 and for the two extreme temperatures, whereas the curves are very close for saturation degrees greater than 0.7. Overall, the effects of a temperature increase are then to decrease the capillary pressure for a given saturation degree, and appears thus to be dominated by the variations (decrease) of σ_{gl} and ρ_l with T. It can be deduced that a moderate increase in temperature in the range of a few tens of degrees from the ambient condition does not affect importantly the capillary pressure curve, in particular for high saturation degrees.

6. Evaluation of the isotherm adsorption curve

This section is devoted to the estimation of the isotherm adsorption curve $S_r(h_r)$ for cementitious materials with the model developed in the preceding sections. The term 'isotherm' indicates that this curve is given for a specified value of temperature T, and consequently a most general notation is $S_r(h_r, T)$. The effects such as ink bottle and pore-blocking (see e.g. [33–35]), leading to hysteresis loop in the $S_r(h_r, T)$ curves when the material is submitted alternatively to adsorption and desorption (wetting–drying paths), are not considered here. In practice, the function $S_r(h_r, T)$ is generally used to calculate the $p_c(S_r)$ (or more precisely $p_c(S_r, T)$) curves via the use of the Kelvin's law in the models involving water transfers in unsaturated conditions. The major reason is that it can be, contrary to $p_c(S_r, T)$, determined by a simple, though often time-consuming, experimental procedure. Combining Eqs. (25)–(30) yields explicitly:

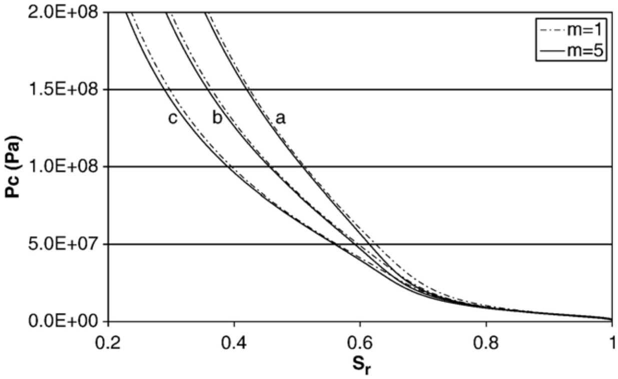

Fig. 10. Evolutions of $p_c(S_r)$ for Material 1 and the two cases $m=1$ and $m=5$, when the adsorbed water layer thickness t is included in the calculation of both S_r and h_r (a), when it is included only in the calculation of S_r (b), and when it is supposed to be 0 (c).

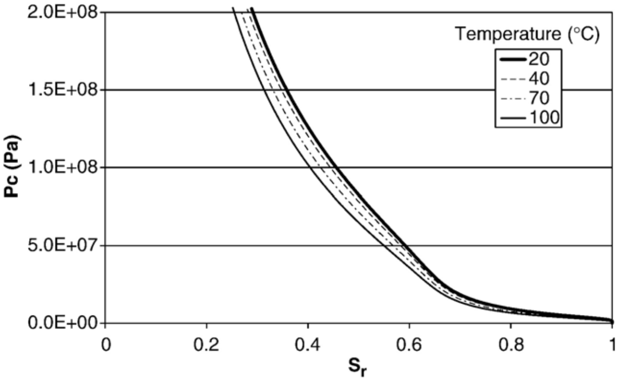

Fig. 11. Evolutions of $p_c(S_r)$ for Material 1 with $m=5$, for several values of temperature.

$$S_r(h_r, T) = \frac{1}{\phi_1^0}\left[e_v\left(\frac{2\sigma_{gl}M_v}{\rho_l RT \ln h_r} - t(h_r)\right) - \left(1-\phi_1^0\right)\right] \tag{31}$$

In addition to $S_r(h_r, T)$, it is also of practical interest for water transfer modeling in non-isothermal conditions (for example in the case of thermo-hydromechanical problems, see e.g. [24–26]) to have an explicit expression of both $\partial S_r/\partial h_r$ and $\partial S_r/\partial T$, since these terms enter into the formulation of the mass conservation equation for water (alternatively, $\partial S_r/\partial h_r$ may be replaced by $\partial S_r/\partial p_c$, depending on the variable retained for describing the water state). Due to the explicit form (31) and with the help of Eq. (3) relating the nearest-surface distribution function $h_v(r)$ to the void exclusion probability $e_v(r)$, we have:

$$\frac{\partial S_r(h_r, T)}{\partial h_r} = \frac{h_v(h_r, T)}{\phi_1^0}\left[\frac{\delta(h_r, T)}{h_r \ln h_r} + t'(h_r)\right]$$

$$\frac{\partial S_r(h_r, T)}{\partial T} = \frac{\delta(h_r, T) h_v(h_r, T)}{\phi_1^0}\left[\frac{\rho'_l(T)}{\rho_l(T)} + \frac{1}{T} - \frac{\sigma'_{gl}(T)}{\sigma_{gl}(T)}\right] \tag{32}$$

where the classical notation $f'(x) = \mathrm{d}f(x)/\mathrm{d}x$ is adopted. The compact expressions of $\partial S_r/\partial h_r$ and $\partial S_r/\partial T$ in Eq. (32) makes use of Eq. (25) giving δ as a function of h_r and T as $\delta(h_r, T) = 2\sigma_{gl}/p_c = -2\sigma_{gl}M_v/(\rho_l RT \ln h_r)$. Interestingly, the first relation of (32) may take the alternative form:

$$\begin{aligned}\frac{\partial S_r(p_c, T)}{\partial p_c} &= \frac{\partial S_r(p_c, T)}{\partial h_r}\frac{\partial h_r}{\partial p_c}\\ &= \frac{h_v(p_c, T)}{\phi_1^0 p_c}\left[\delta(p_c, T) + t'(h_r) h_r \ln h_r\right]\end{aligned} \tag{33}$$

since we have $\partial h_r/\partial p_c = h_r \ln h_r / p_c$. Eqs. (31) and (32) then provide explicit expressions of the isotherm adsorption curves and their derivatives with respect to their arguments h_r and T (or p_c and T). These expressions incorporate microstructural information via the description of the pore network by a polydispersed overlapping sphere system; for this (very) idealistic pore representation, the results obtained are exact.

The three model materials defined in Section 4 for illustrating and evaluating the global capacities of the proposed method are again used in this section. Fig. 12 then presents the numerical results obtained for $S_r(h_r, T=20\ °\mathrm{C})$ with $m=1$ and $m=5$. As expected, the remarks formulated for the capillary pressure curves can be globally applied to the case of the adsorption curves. Indeed, it appears again clearly that the pore size distribution affects non-negligibly the $S_r(h_r, T)$ function. Whereas the curves of Materials 1 and 2 appear relatively close, indicating that the porosity is not the most significant factor impacting the adsorption curve, the results obtained for Material 3 show important differences in both shape and magnitude of the curve. This illustrates that the effects of the size of the pore classes are of particular importance regarding the adsorption curve. In fact, this is not surprising since h_r depends directly on the pore radius via the capillary pressure. Hence, modifying the porosity volume fraction corresponding to pore sizes greater than a given pore radius is equivalent to changing the saturation degree for a given relative humidity. The influence domain of each pore class appears clearly on the simulated curves; indeed, the concave portions of these latter are related to the concave parts of the $V(\delta)$–δ curves for the same materials (see Fig. 6), which are centered on the average pore class radius. The respective volume fraction of these pore classes can also be roughly identified on the adsorption curves by considering that the transition between two pore classes is indicated by the $S_r(h_r, T)$ curvature change from convex to concave. This change appears around $S_r=0.65$ and $S_r=0.75$ for Material 1 and Material 2, respectively, which is consistent with the respective porosity volume fraction of about 35% and 25% for the greater pore size class. In addition, it can be noticed that the obtained curves agree well with the experimental data of adsorption curves reported in [22] for three cement pastes having different compositions ranging from high performance material, to be related to Material 2 of this study, to weak performance one with pore size characteristics relatively close to those of Material 3. To conclude, the proposed model, which includes basic microstructural information in the description of the pore space, is able to provide a quantitative estimation of the isotherm adsorption curve.

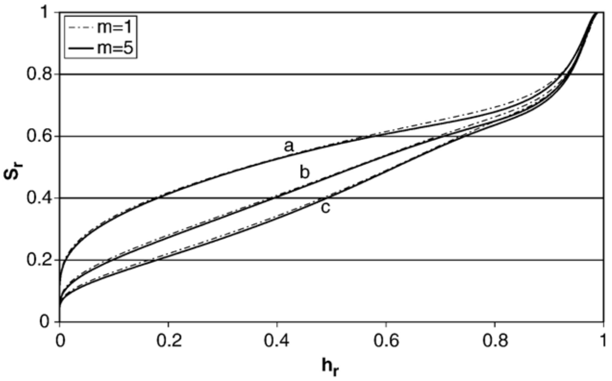

Fig. 13. Evolutions of $S_r(h_r)$ for Material 1 and the two cases $m=1$ and $m=5$, when the adsorbed water layer thickness t is included in the calculation of both S_r and h_r (a), when it is included only in the calculation of S_r (b), and when it is supposed to be 0 (c).

As in the case of the $p_c(S_r, T)$ curves, to illustrate the influence of the thickness of the adsorbed water layer t on $S_r(h_r, T)$, we present in Fig. 13 the evolutions of the adsorption curves for Material 1 in the following configurations: t is included in the calculations for both h_r and S_r (a), t is only included in the expression of S_r (b), and t is considered to be 0 (c). Again, the configuration (b) results from the model as presented in this paper, whereas (a) is a virtual situation in which δ is replaced by $\delta - t$ in the Laplace equation. Similarly to the $p_c(S_r, T)$ curve, the influence of the thickness t appears noticeable, except for high saturation degrees ($S_r > 0.8$–0.9, or equivalently $\delta \gg t$) where it becomes very low (it vanishes for $S_r=1$). It is then clear that t cannot be neglected in general in the adsorption curve estimations. To conclude this section, we evaluate numerically the impact of a moderate temperature increase on the $S_r(h_r, T)$ function. Fig. 14 then shows the simulated results obtained for

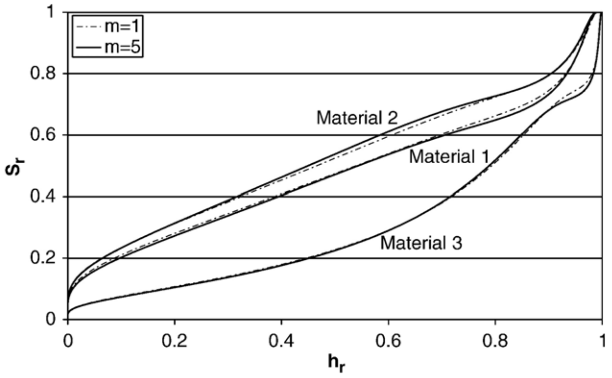

Fig. 12. Evolutions of $S_r(h_r)$ for the three model materials and the two cases $m=1$ and $m=5$.

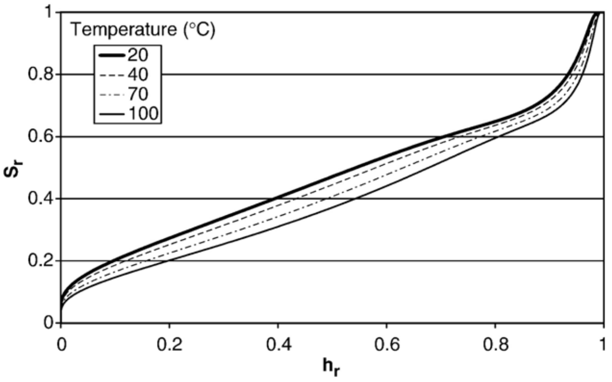

Fig. 14. Evolutions of $S_r(h_r)$ for Material 1 with $m=5$, for several values of temperature.

several temperatures ranging from 20 to 100 °C, for Material 1 with $m=5$. Similarly to a rise of average radii for all pore size classes, a temperature increase leads globally to a reduction of saturation degree at a given h_r. The effects of this parameter appear to be comparatively more marked for the $S_r(h_r, T)$ curves than for the $p_c(S_r, T)$ ones presented in the previous section, and are clearly non-negligible, even for high saturation degrees.

7. Conclusion

This paper proposes to describe the porosity of cementitious materials in terms of pore size distribution by means of a 3-dimensional overlapping sphere system with polydispersivity in size. On the basis of results established by Lu and Torquato [1] providing relations for the nearest-neighbor distribution functions defined as the probability of finding a nearest neighbor at some given distance from a reference point in this system, the volume fraction of pores having a radius larger than a prescribed value is explicitly expressed. Then, by choosing an appropriate size distribution function, experimental pore size distributions such as those given by MIP or nitrogen adsorption, which typically point out several pore domains for cementitious materials, can be reproduced.

Adopting the hypothesis of a spherical water–gaseous interface, the saturation degree is further expressed as a function of the meniscus radius δ and the thickness t of the adsorbed water layer, with the assumption that all pores with radius smaller than $\delta - t$ are filled with water, whereas the others are empty of free water. The resulting relations are then applied to the simulation of the capillary pressure curve $p_c(S_r)$ as a function of the saturation degree; to this end, three model materials with different pore size characteristics are considered. It is then shown that, as expected, the pore size distribution has a deep impact on the magnitude of the capillary pressure at a given saturation level. Similar conclusions are obtained concerning the simulation of the saturation degree versus relative humidity curves $S_r(h_r)$. The effects of a moderate temperature increase (up to 100 °C) on both $p_c(S_r)$ and $S_r(h_r)$ curves are also assessed; it appears that the repercussions resulting from this change are limited but should be considered for an accurate description of these functions. It follows that in practical applications for which transfer phenomena are essential, the dependence of the capillary pressure and relative humidity upon the saturation degree should be precisely characterized as a function of the pore structure, in particular when the latter evolves (for example in thermo-hydromechanical and chemically induced degradation problems).

The application of the model as presented do not yield fundamentally new results; the major contribution of the paper rather resides in providing a quantitative method based on explicit exact relations, corresponding to an actual 3D overlapping sphere system representation of porosity, for estimating some key parameters regarding the water transfer in unsaturated conditions. The main orientations for improving the model concern the problem of hysteresis loops appearing in the adsorption–desorption curves, and the assessment of permeability and diffusion coefficient for both liquid and gaseous phases as a function of S_r.

References

[1] B. Lu, S. Torquato, Nearest-surface distribution functions for polydispersed particle systems, Phys. Rev., A 45 (8) (1992) 5530–5544.

[2] S. Torquato, Random Heterogeneous Media: Microstructure and Macroscopic Properties, Springer-Verlag, New York, 2001.

[3] A. Lioure, B. Porzio, P. Jaecki, C. Moitrier, I. Tirel, C. Villard, C. Leroy, A. Marvy, D. Iracane, Long-term interim storage of thermal HLW: importance, constraints and principles for the management of long times in storage, Int. Conf. GLOBAL 2001, Paris, 2001.

[4] M.C.R. Farage, J. Sercombe, C. Gallé, Rehydration and microstructure of cement paste after heating at temperatures up to 300 °C, Cem. Concr. Res. 33 (2003) 1047–1056.

[5] Guang Ye, Percolation of capillary pores in hardening cement pastes, Cem. Concr. Res. 35 (2005) 167–176.

[6] J. Hu, P. Stroeven, Depercolation threshold of porosity in model cement: approach by morphological evolution during hydration, Cem. Concr. Compos. 27 (2005) 19–26.

[7] E.J. Garboczi, D.P. Bentz, The effect of statistical fluctuation, finite size error, and digital resolution on the phase percolation and transport properties of the NIST cement hydration model, Cem. Concr. Res. 31 (2001) 1501–1514.

[8] E.J. Garboczi, K.A. Snyder, J.F. Douglas, M.F. Thorpe, Geometrical percolation threshold of overlapping ellipsoids, Phys. Rev., E 52 (1995) 819–828.

[9] H.M. Jennings, A model for the microstructure of calcium silicate hydrate in cement paste, Cem. Concr. Res. 30 (2000) 101–116.

[10] P.D. Tennis, H.M. Jennings, A model for two types of calcium silicate hydrate in the microstructure of Portland cement pastes, Cem. Concr. Res. 30 (2000) 855–863.

[11] D.W. Hadley, W.L. Dolch, S. Diamond, On the occurrence of hollow-shell hydration grains in hydrated cement paste, Cem. Concr. Res. 30 (2000) 1–6.

[12] J. Quintanilla, Measures of clustering in systems of overlapping particles, Mech. Mat. 38 (2006) 849–858.

[13] F.A.L. Dullien, Porous Media. Fluid Transport and Pore Structure, Academic Press, Inc., 1989.

[14] R. Vočka, C. Gallé, M. Dubois, P. Lovera, Mercury intrusion porosimetry and hierarchical structure of cement pastes. Theory and experiments, Cem. Concr. Res. 30 (2000) 521–527.

[15] S. Diamond, Mercury porosimetry. An inappropriate method for the measurement of pore size distributions in cement-based materials, Cem. Concr. Res. 30 (2000) 1517–1525.

[16] S.P. Rigby, A hierarchical structural model for the interpretation of mercury porosimetry and nitrogen sorption, J. Colloid Interface Sci. 224 (2000) 382–396.

[17] S.P. Rigby, R.S. Fletcher, S.N. Riley, Determination of the multiscale percolation properties of porous media using mercury porosimetry, Ind. Eng. Chem. Res. 41 (2002) 1205–1226.

[18] K.A. Snyder, A numerical test of air void spacing equations, Adv. Cem. Based Mater. 8 (1998) 28–44.

[19] E.J. Garboczi, D.P. Bentz, Analytical formulas for interfacial transition zone properties, Adv. Cem. Based Mater. 6 (1997) 99–108.

[20] H.F.W. Taylor, in: Thomas Telford (Ed.), Cement Chemistry, second ed., London, 1997.

[21] C. Gallé, H. Peycelon, P. Le Bescop, Effect of an accelerated chemical degradation on water permeability and pore structure of cement-based materials, Adv. Cem. Res. 16 (3) (2004) 105–114.

[22] V. Baroghel-Bouny, Caractérisation des pâtes de ciment et des bétons. Méthodes, analyse et interprétations (1994), PhD thesis (in French), LCPC.

[23] O. Coussy, Mechanics of Porous Continua, Wiley, New York, 1995.

[24] D. Gawin, F. Pesavento, B.A. Schrefler, Modelling of hygro-thermal behaviour and damage of concrete at temperature above the critical point of water, Int. J. Numer. Anal. Methods Geomech. 26 (2002) 537–562.

[25] R.W. Lewis, B.A. Schrefler, The Finite Element Method in the Static and Dynamic Deformation and Consolidation of Porous Media, Wiley, New York, 1998.

[26] J. Rutqvist, L. Börgesson, M. Chijimatsu, A. Kobayashi, L. Jing, T.S. Nguyen, J. Noorishas, C.-F. Tsang, Thermohydromechanics of partially saturated geological media: governing equations and formulation of four finite element models, Int. J. Rock Mech. Min. Sci. 38 (2001) 105–127.

[27] B. Bary, A. Sellier, Coupled moisture–carbon dioxide–calcium transfer model for carbonation of concrete, Cem. Concr. Res. 34 (2004) 1859–1872.

[28] W.G. Gray, B.A. Schrefler, Thermodynamic approach to effective stress in partially saturated porous media, Eur. J. Mech. A, Solids 20 (2001) 521–538.

[29] R. Černý, P. Rovnaníková, Transport Processes in Concrete, Spon Press, 2002.

[30] J.J. Hagymassy, S. Brunauer, R.S. Mikhail, Pore structure analysis by water vapour adsorption–*t*-curves for water vapour, J. Colloid Interface Sci. 29 (3) (1969) 485–491.

[31] B. Le Neindre, Tensions superficielles des composes inorganiques et des mélanges, Tech. Ing., Constantes Méc. K3 (1993).

[32] K. Ranznjevic, Tables et Diagrammes Thermodynamiques, Eyrolles, 1970.

[33] L. Sarkisov, P.A. Monson, Modeling of adsorption in pores of simple geometry using molecular dynamics, Langmuir 17 (2001) 7600–7604.

[34] P.I. Ravikovitch, A.V. Neimark, Experimental confirmation of different mechanisms of evaporation from ink-bottle type pores: equilibrium, pore blocking, and cavitation, Langmuir 18 (2002) 9830–9837.

[35] A. Vishnyakov, A.V. Neimark, Monte Carlo simulation test of pore blocking effects, Langmuir 19 (2003) 3240–3247.